

# Accelerating Carbon Capture and Storage Modeling using Fourier Neural Operators

Gege Wen<sup>1,\*</sup>, Zongyi Li<sup>2</sup>, Qirui Long<sup>1</sup>, Kamyar Azizzadenesheli<sup>3</sup>, Anima Anandkumar<sup>2,3</sup>, and Sally M. Benson<sup>1</sup>

<sup>1</sup>Energy Sciences and Engineering, Stanford University, Stanford, 94305, CA, USA

<sup>2</sup>Computing and Mathematical Sciences, California Institute of Technology, Pasadena, 91125, CA, USA

<sup>3</sup>NVIDIA Corporation, Santa Clara, 95051, CA, USA

\*corresponding author: gegewen@stanford.edu

Carbon capture and storage (CCS) is an important strategy for reducing carbon dioxide emissions and mitigating climate change. We consider the storage aspect of CCS, which involves injecting carbon dioxide into underground reservoirs. This requires accurate and high-resolution predictions of carbon dioxide plume migration and reservoir pressure buildup. However, such modeling is challenging at scale due to the high computational costs of existing numerical methods. We introduce a novel machine learning approach for four-dimensional spatial-temporal modeling, which speeds up predictions nearly 700,000 times compared to existing methods. It provides highly accurate predictions under diverse reservoir conditions, geological heterogeneity, and injection schemes. Our framework, Nested Fourier Neural Operator (FNO), learns the solution operator for the family of partial differential equations governing the carbon dioxide-water multiphase flow. It uses a hierarchy of FNO models to produce outputs at different refinement levels. Thus, our approach enables unprecedented real-time high-resolution modeling for carbon dioxide storage.

## Main

Carbon capture and storage (CCS) is the process of capturing carbon dioxide and permanently storing it in subsurface geological formations to mitigate climate change<sup>1</sup>. We consider the storage modeling of CCS, which involves the multiphase flow of carbon dioxide and water through porous media. Numerical simulations are used to guide critical engineering decisions in CCS projects by forecasting carbon dioxide gaseous plume migration in the formation and pressure buildup caused by the injection.

Current numerical simulations are very expensive due to the multi-scale and multi-physics modeling involved, the high-resolution grids required, and the large spatial-temporal ranges needed for real-world scenarios. The governing partial differential equations (PDEs) involving the multiphase variation of Darcy’s law are expensive to solve<sup>2,3</sup>. Carbon dioxide and water are immiscible and mutually soluble, requiring multi-physics simulation coupled with thermodynamics<sup>4</sup>. High-resolution spatial grids (1-2 m resolution) are necessary to provide accurate estimates of the carbon dioxide plume migration, which is controlled by the complex interplay of buoyancy, viscous, and capillary forces<sup>5,6</sup>. Pressure buildup, as well as the dry-out effect, i.e., evaporation of forma-

tion fluid into the gas phase<sup>7,8</sup>, also demand particularly high resolutions around the injection well. In real-world scenarios, CCS projects often involve large reservoir spatial domains of hundreds of kilometers<sup>9</sup> and long time frames that span from decades to hundreds of years<sup>10</sup>.

One approach for reducing the computational costs of numerical simulations is to use non-uniform grids to capture different responses at different grid resolutions. A popular method, known as local grid refinement<sup>11</sup> (LGR), has enabled scaling simulations to real-world three-dimensional (3D) carbon dioxide storage projects, where the fine-grid responses capture the plume migration while the coarser grid responses capture the far-field pressure buildup<sup>12–14</sup>. However, even with non-uniform grid approaches, these numerical models are still too expensive for tasks that require repetitive forward simulations, e.g., site selection<sup>15</sup>, inversion<sup>16</sup>, or optimization<sup>17,18</sup>. In practice, these numerical simulation methods are forced to reduce computational costs by coarsening the grid resolution<sup>19</sup> and/or simplifying the physics<sup>20</sup>, which reduces the accuracy of modeling.

In recent years, machine learning (ML) approaches are emerging as a promising alternative to numerical simulation for subsurface flow problems<sup>21–25</sup>. ML methods are usually much faster than numerical simulators because the inference is very cheap once the ML models

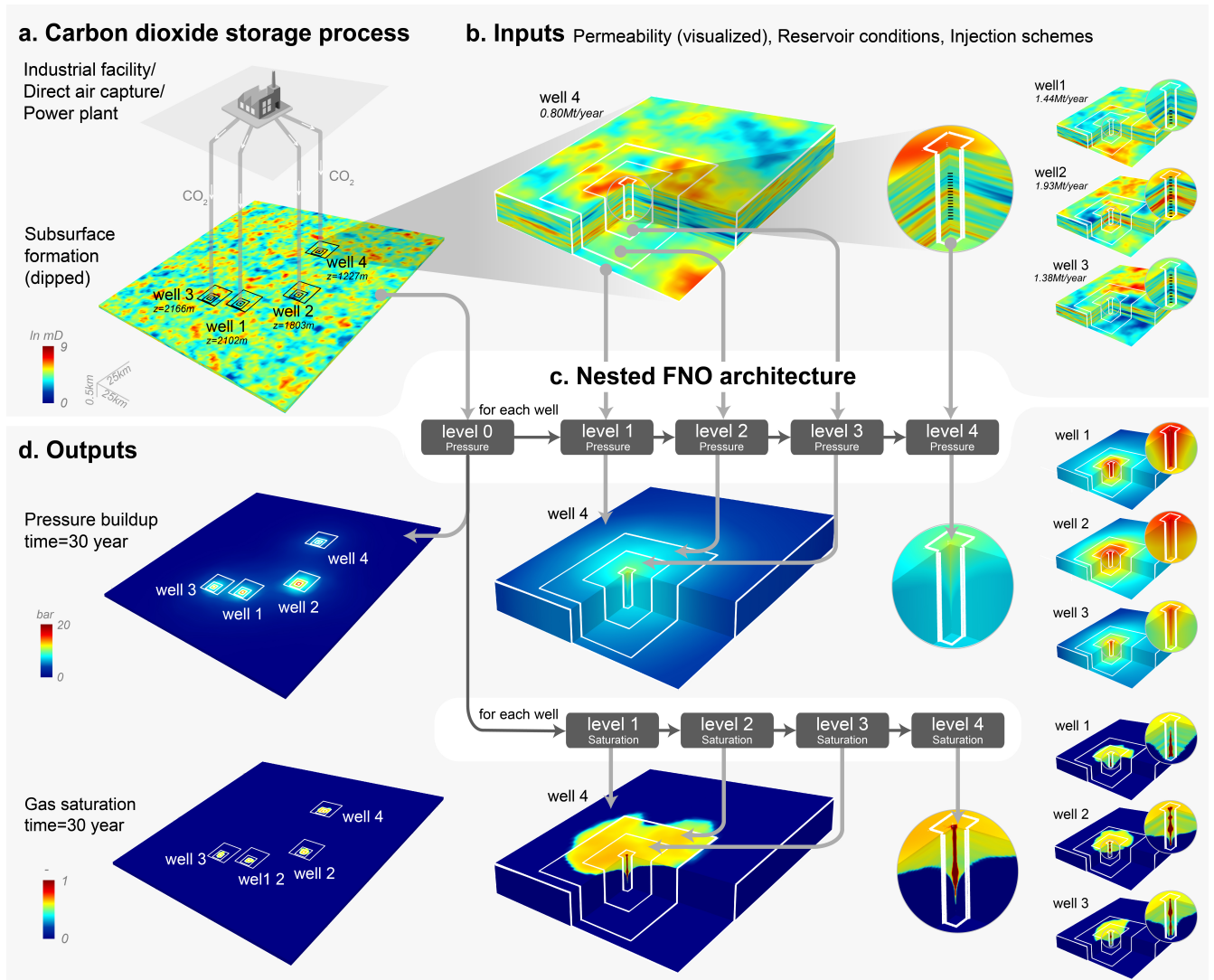


**Figure 1. Introduction to Nested-FNO.** a-b. Permeability for a dipped 3D reservoir with four injection wells; white and black lines indicate level 0 to 4's boundary; the black dotted lines in the zoomed-in circles show the locations of injection perforation intervals. c. Each grey block represents an FNO model; light grey arrows point to the input and output's level; dark grey arrows show when one model's output is used as another model's input. Notice we feed level 0 pressure buildup output to level 1 gas saturation model because carbon dioxide plumes never migrate to level 0. d. Pressure buildup and gas saturation at 30 years.

are trained. However, standard ML methods suffer from the lack of generalization and fail to provide accurate estimates away from the domain of training data. This limits the usage of ML in challenging applications such as carbon dioxide storage modeling because it requires generalization under diverse geology, reservoir conditions, and injection schemes. A recent machine-learning framework, termed neural operators<sup>26–28</sup>, overcomes these generalization challenges by directly learning the solution operator for the PDE system family instead of

just learning a single instance. By learning the solution operator, neural operators generalize well to different conditions in the PDE system as well as discretizations without the need for re-training the ML model.

Fourier neural operator (FNO) is a class of neural operators that uses Fourier transform to learn the solution operator<sup>29</sup> efficiently. A variant of FNO was previously used in carbon dioxide storage modeling<sup>30</sup> that showed 60,000 times speedup and excellent generalization. This previous model<sup>30</sup> is limited to a 2D spatial domain that

can only represent flat reservoirs with a single injection well. However, In real-world scenarios, CCS projects often involve multiple injection wells and dipped reservoirs. Due to the buoyancy effect, reservoir dipping angles can significantly influence the gaseous plume migration. These processes can only be accurately captured by high-resolution 3D spatial domains, where the costs of collecting training data from numerical solvers become prohibitive. We incorporate these practical modeling features in the current work.

Here, we present an ML approach with unprecedented capabilities of high-resolution 4D spatial-temporal modeling of pressure buildup and gas saturation for realistic carbon dioxide storage projects. We integrate the FNO architecture with the LGR modeling approach to obtain a Nested Fourier Neural Operator (Nested FNO) architecture. As shown in Figure 1, five levels of FNOs are used to predict outputs in five levels of grid refinements; each coarser-level model's output is used as the finer-level model's input. This nested approach vastly reduces the computational cost needed during data collection and overcomes the memory constraints in model training. For instance, Nested FNO only needs less than 2,500 training data at the coarsest resolution (level 0) and about 6,000 samples for the finer levels (1-4). Despite the small training size, Nested FNO generalizes well to large problem dimensions with millions of cells. The spatial resolutions provided by Nested FNO are finer than most current simulations run with existing numerical models (e.g., Sleipner benchmark model<sup>31</sup> and Decatur model<sup>32</sup>). Nested FNO provides 700,000 times speedup. The fast inference enables rigorous probabilistic assessments for maximum pressure buildup and carbon dioxide plume footprint. Such assessments are important for decisions on injection design and land lease acquisition. Running such assessments take nearly two years with traditional simulators, and it took only 2.8 seconds with the Nested FNO model.

## Results

We consider carbon dioxide injection into dipped 3D reservoirs through multiple wells over 30 years, as shown in Figure 1 a. Our data set considers a comprehensive collection of input variables for practical carbon dioxide storage projects, covering most realistic scenarios of potential sites. Each input variable is sampled according to expert knowledge, including reservoir conditions (depth, temperature, dip angle), injection schemes (num-

ber of injection wells, rates, perforation intervals), and permeability heterogeneity (mean, standard deviation, correlation lengths). See *Supplementary, Data set generation* for details for the input variable sampling.

## Prediction accuracy

### Gas saturation

The migration of carbon dioxide plumes is governed by the complex interplay of viscous, capillary, and gravity forces. Due to the presence of the dip angle, the reservoir condition around each well can lead to various fluid properties in the same reservoir. In addition, carbon dioxide plumes can form distinctively different shapes and sizes according to different injection schemes and permeability heterogeneity.

As shown in Figure 2 a, Nested FNO captures these complex processes with excellent accuracy. Near the injection perforation interval, we observe dry-out zones where the gas saturation is near one, e.g., at the bottom half of well 1. This is a highly nonlinear response caused by the vaporization of the formation fluids into the gas phase<sup>7</sup>. This important physical process is neglected by many numerical models because it can only be captured with high grid resolutions and high-fidelity simulations. Nevertheless, Nested FNO predicts the dry-out with high accuracy. We observe slightly more errors at the plumes and dry-out zones' edges. This is because the simulation data around discontinuous saturation transitions consist of inherent numerical artifacts that are less systematic.

Overall, Nested FNO displays small overfitting considering the problem's high dimensionality (Figure 2 d). The average saturation error ( $\delta_S$ ) for the gaseous carbon dioxide plume is 1.2% for the training set and 1.8% for the testing set. See *Methods* for  $\delta_S$ 's definition. This accuracy is sufficient for practical applications such as forecasting plume footprints and estimating sweep efficiencies.

### Pressure buildup

As demonstrated in Figure 3 a, Nested FNO precisely captures the local pressure buildup responses around each well, as well as the global interaction among them. The high resolution provides accurate estimates of the maximum pressure buildup, which is an essential indicator of reservoir integrity. The global level prediction provides the spatial extent of the region of pressure buildup influence, another important parameter required for regulatory purposes<sup>33</sup>. Additionally, Figure 3 a-c shows that accuracy is consistent across different predic-

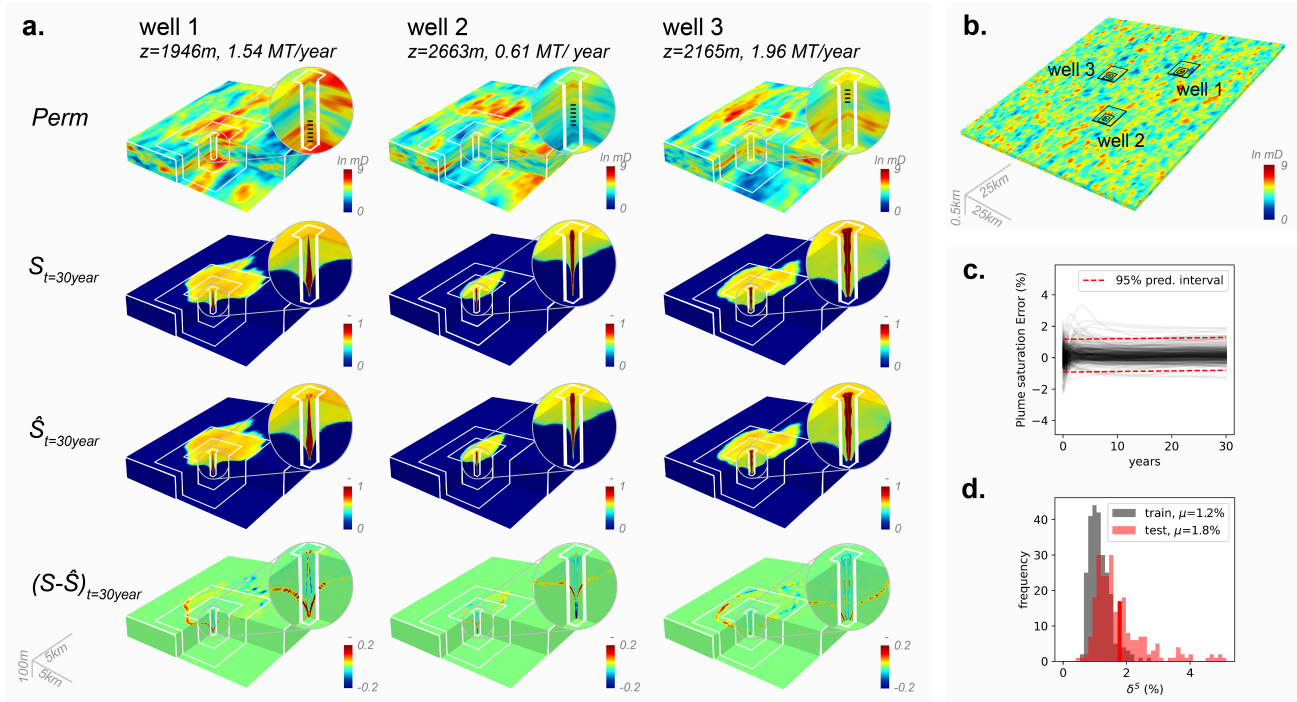


**Figure 2. Gas saturation prediction.** **a.** Visualizations of gas saturation predictions at 30 years for a 3-well case. Each row shows permeability, gas saturation ground truth, prediction, and error. The white lines indicate the boundary between each level. **b.** Reservoir permeability and the location of each well. **c.** Testing set plume saturation error versus time for 250 random cases. The red dotted line shows the 95% prediction bands of the error. **d.** Error histograms for 250 cases in the training and test set. The solid red column indicates the error for the shown example.

tion domains and throughout the injection period. These predictions are sufficient to guide important engineering decisions such as injection schemes and monitoring program designs.

The relative pressure buildup error  $\delta^P$  (as defined in *Methods*) for the training and the testing set are 0.3% and 0.5%, respectively. Similar to the gas saturation, we observe small overfitting from the error histogram (Figure 3 d) for the training and testing set. This generalization is remarkable, considering the training data size for this high-dimensional problem. The generalizability is achieved through a fine-tuning technique which we will introduce in *Methods*.

### Computational Speed-up

Once the Nested FNO model is trained, we can use it as a general-purpose numerical simulator alternative in realistic 3D reservoirs. This approach allows traditional users to skip numerical simulations for an entire class of problems and directly obtain efficient, high-fidelity, and

high-resolution predictions<sup>25</sup>. Our approach differs from the task-specific “surrogate” modeling approach, which often involves a specific set of reservoir conditions.

As a result, we calculate the computational speedup by comparing the Nested FNO’s prediction time to the numerical simulation run time of a state-of-the-art full-physics simulator ECLIPSE<sup>34</sup>. Each model in Nested FNO takes about 0.005s to infer, while the total prediction time depends on the number of injection wells. On average, the Nested FNO provides 400,000 (1-well case) to 700,000 (4-well case) times speedup compared to traditional simulation. Refer to *Supplementary, Speedup analysis* for detailed specifications for the simulator and ML models.

### Probabilistic assessment

Nested FNO’s fast prediction speed enables rigorous probabilistic assessments that were previously unattainable. As an example, we investigate the maximum pressure buildup and carbon dioxide plume footprint for a



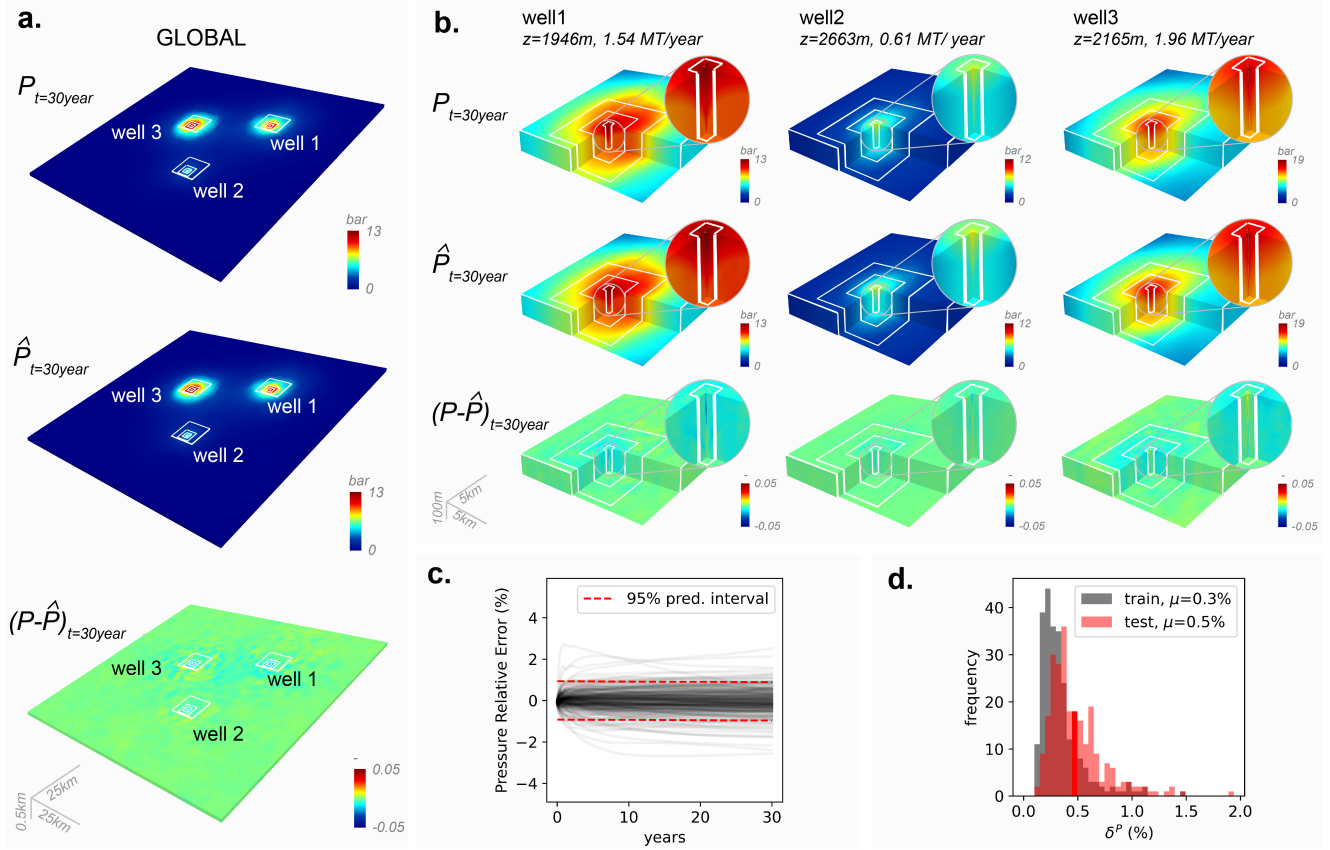


**Figure 3. Pressure buildup prediction.** **a.** Global and **b.** well pressure buildup predictions at 30 years. Each row shows pressure buildup ground truth, prediction, and relative error. The white lines indicate the boundary between each level. **c.** Testing set pressure relative error versus time for 250 random cases. The red dotted line shows the 95% prediction bands of the error. **d.** Error histograms for 250 cases in the training and test set. The solid red column indicates the error for the visualized example.

four-well reservoir where each well injects at a 1MT/year rate. Refer to *Supplementary, Probabilistic assessment* for detailed setups. We generate 1,000 permeability realizations using the same distribution and spatial correlations, then use Nested FNO to predict gas saturation plumes and pressure buildup for each realization. As shown in Figure 4, the probabilistic estimates of the carbon dioxide plume footprint and maximum pressure buildup can support project developers and regulators in making important engineering decisions<sup>35</sup>. For example, the plume footprint helps determine the area of the land lease acquisition required and the monitoring program's design<sup>10</sup>; the maximum reservoir pressure buildup helps evaluate the safety of an injection scheme and ensure reservoir integrity. Running such assessments takes nearly two years with traditional numerical simulators, and it takes only 2.8 seconds with Nested FNO.

## Discussion

We present the Nested FNO model for high-resolution 4D gas saturation and pressure buildup in CO<sub>2</sub> storage problems. The trained model provides exceptionally fast predictions and can support many engineering tasks that require repetitive forward simulations, including but not limited to (1) probabilistic assessment - as demonstrated above, (2) site selection<sup>15</sup> - quick screening for a large number of potential reservoirs, (3) storage optimizations<sup>18,36</sup> - exhaustive search in the parameter space, and (4) seismic inversion<sup>37</sup> - provide forward simulation outputs and gradients. Nested FNO can readily serve as a high-fidelity and high-resolution numerical simulator alternative and facilitate rigorous analyses for these tasks.

A highlight of the Nested FNO is its excellent gen-

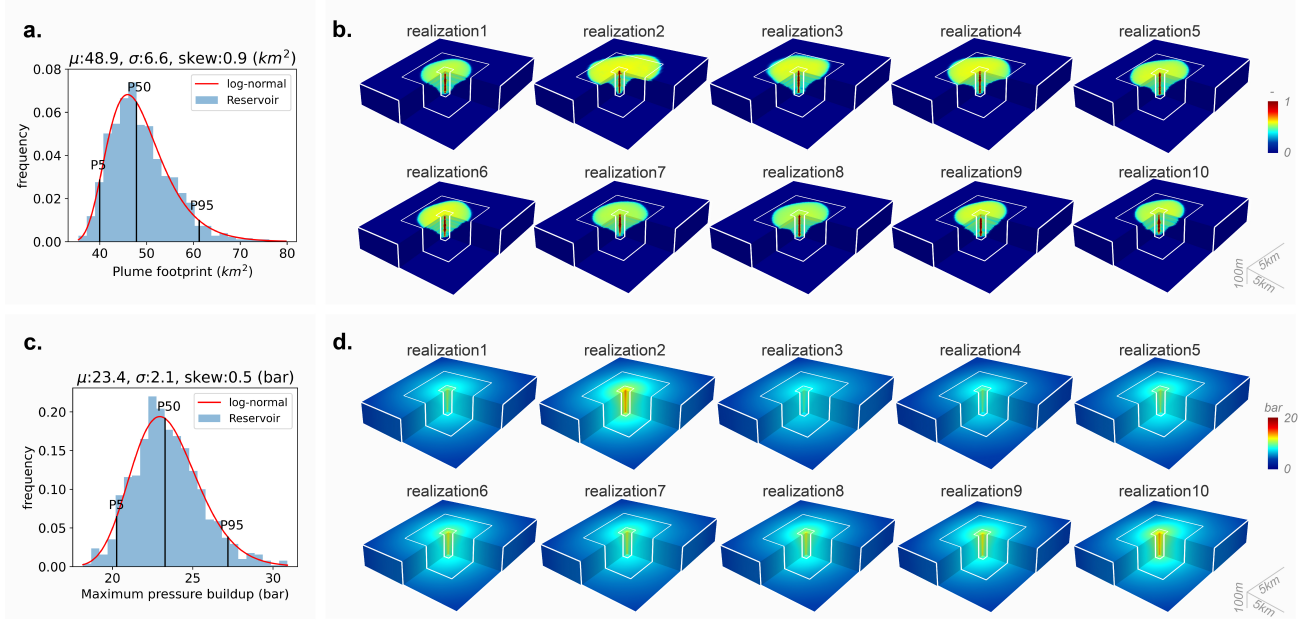


**Figure 4. Probabilistic assessment.** **a.** Histogram of CO<sub>2</sub> plume footprint predictions given 1,000 permeability realizations from the same geological parameters. The result satisfies a log-normal distribution; P5, P50, and P95 are marked on the distribution. **b.** Ten realizations of CO<sub>2</sub> plume at 30 years. **c.** Histogram of CO<sub>2</sub> pressure buildup predictions given the same 1,000 permeability realizations. The result satisfies a log-normal distribution; P5, P50, and P95 are marked on the distribution. **d.** Ten realizations of pressure buildup at 30 years.

eralizability. The training sizes for Nested FNO are small (2,408 for the level 0 model and 5,916 for level 1-4 models), considering the large problem dimension with millions of cells. We achieve this generalizability through (1) a novel fine-tuning technique for nested architecture as introduced in *Methods* and (2) the utilization of the FNO architecture. Most existing machine learning approaches for subsurface flow use convolutional neural network (CNN)-based models with local kernels and deep architectures that are prone to overfitting<sup>38–42</sup>. Unlike CNN, FNO uses global kernels to learn an infinite-dimensional input and output mapping in the function space<sup>29</sup>. Our previous study shows that FNO-based models require only one-third of the training data compared to the CNN-based model in a 2D spatial-temporal setting<sup>30</sup>. As a result, using FNO greatly reduces the demand for training data; combining FNO with the LGR approach makes this high-resolution 3D problem tractable.

Besides data-driven approaches, another line of work, often referred to as a physics-informed neural network, attempts to solve the governing PDE by parameterizing governing relations and initial/boundary conditions using neural networks<sup>43</sup>. However, these approaches

have not yet shown significant advantages in computational efficiency for subsurface multiphase flow through heterogeneous media<sup>44–47</sup>. On the contrary, as a data-driven approach, Nested FNO provides a framework with great potential not only for CO<sub>2</sub> storage but also for other scientific problems that involve multi-level modeling. For instance, in weather forecast modeling, different cyclones can develop locally while interacting with each other on a global level<sup>48</sup>; in nuclear fusion, the collision of multiple nuclei in a particle involves long-distance interactions as well as inner-nucleus many-particle physics<sup>49</sup>.

## Methods

Refer to *Supplementary* for detailed descriptions of the governing PDEs and numerical simulation setups.

## Data overview

The data set is generated using a semi-adaptive LGR approach to ensure both high fidelity and computational tractability. We use the global (level 0) resolution grid in the large spatial domain to mimic typical saline storage formations with infinite boundary conditions. Next, we apply four levels of local refinements (levels 1 to 4)

around each well to gradually increase the grid resolutions. Going from levels 0 to 4, we reduce the cell size by 80x on the  $x, y$  dimensions and 10x on the  $z$  dimension to resolve near-well plume migration, dry-out, and pressure buildup. See *Supplementary, Local Grid Refinement* for details on the LGR design.

### Nested FNO architecture

Nested FNO uses a sequence of FNO models to predict the data set with multiple refinement levels. The computational domain of the Nested FNO is a 3D space with time,  $D = \Omega \times T$ , where  $T$  is the time interval of 30 years and  $\Omega$  is the reservoir domain. As shown in Figure 1, the 3D reservoir domain consists of subdomains  $\Omega_i$  at levels 0 to 4 for each grid refinement. We use nine FNO models:  $\mathcal{G}_{0..4}^P$  for pressure buildup ( $P$ ), and  $\mathcal{G}_{1..4}^S$  for gas saturation ( $S$ ), to predict outputs at each level. We extend the original FNO<sup>29</sup> architecture into 4D to produce outputs in the 3D space-time domain. See *Supplementary, Fourier Neural Operator* for detailed architecture and parameters.

The input for each model includes the permeability field, initial hydro-static pressure, reservoir temperature, injection scheme, as well as spatial and temporal encoding. In carbon dioxide-water multiphase flow, pressure buildup travels significantly faster than gas saturation. Therefore, we use  $\mathcal{G}_0^P$  to predict level 0 (global) pressure buildup as well as the pressure interaction between wells. We then feed level 0 pressure buildup prediction around each injection well ( $\hat{P}_0|_{well,j}$ ) to models on level 1. Each subsequent model takes the input on domain  $\Omega_i$  together with the coarser-level prediction of  $\hat{P}$  or  $\hat{S}$  on  $\Omega_{i-1}$ , and outputs the prediction of  $\hat{P}$  or  $\hat{S}$  on  $\Omega_i$ . By giving the coarser-level prediction to the finer-level model as an input, we also provide the boundary conditions of the finer-level subdomain, which significantly improves the finer-level predictions.

### Training procedure

To train the Nested FNO, we first prepare the input-output pairs for each subdomain and train each of the nine models independently. For each model, we use the ground truth, i.e., numerical simulation, pressure buildup and gas saturation on the coarse-level training domain to construct the input. This approach is time efficient because it allows us to train all models concurrently instead of sequentially going from coarser-level to finer-level models. Refer to *Supplementary, Training procedure* for more details.

### Inference procedure

Once we train the nine models in the Nested FNO, we can predict the gas saturation and pressure buildup according to Algorithm 1. Notice that the number of subdomains in  $\Omega$  depends on the number of injection wells. For example, a reservoir with three injection wells has 13 subdomains  $\Omega = \{\Omega_0, \Omega_{level1..4,well1}, \Omega_{level1..4,well2}, \Omega_{level1..4,well3}\}$ . Therefore, we repeat the inference for each injection well. The input can be constructed given any random combination of reservoir condition (depth, temperature, and dip angle), injection scheme (number of wells, rate, location, perforation interval), and permeability field, as long as the variables are within the training data sampling ranges.

---

**Algorithm 1** Predict gas saturation and pressure buildup in a reservoir with  $n$  injection wells.  $\mathcal{G}$  denotes the a model,  $P$  denotes pressure buildup,  $S$  denotes gas situation, and  $a$  denotes input.

---

```

Use  $\mathcal{G}_0^P$  to predict  $\hat{P}_0$  given  $a_0$ 
for each well  $j = 1, \dots, n$  do
    Construct input  $(a_{1,j}, \hat{P}_0|_j)$ 
    Use  $\mathcal{G}_1^P$  and above input to predict  $\hat{P}_{1,j}$ 
    Use  $\mathcal{G}_1^S$  and above input to predict  $\hat{S}_{1,j}$ 
    for each level  $i = 2, \dots, 4$  do
        Construct input  $(a_{i,j}, \hat{S}_{i-1,j})$ 
        Use  $\mathcal{G}_i^S$  and above input to predict  $\hat{S}_{i,j}$ 
        Construct input  $(a_{i,j}, \hat{P}_{i-1,j})$ 
        Use  $\mathcal{G}_i^P$  and above input to predict  $\hat{P}_{i,j}$ 
    end for
end for

```

---

### Evaluation metrics

To evaluate the gas saturation prediction accuracy in reservoirs with multiple levels of refinements, we introduce the plume saturation error  $\delta_S$ , defined as:

$$\delta^S = \frac{1}{\sum_{t,i} I_{t,i}} \sum_{t \in T} \sum_{i \in \Omega} I_{t,i} |S_{t,i} - \hat{S}_{t,i}|, \quad (1)$$

$$I_{t,i} = 1 \quad \text{if} \quad (S_{t,i} > 0.01) \cup (|\hat{S}_{t,i}| > 0.01).$$

$S$  is the ground truth gas saturation,  $\hat{S}$  is the predicted gas saturation,  $T$  includes all times snapshots over the 30 years, and  $\Omega$  includes all the cells as in the original domain of the numerical simulator; refer *Supplementary, Training procedure* for more details. We use this metric because the reservoir domain includes many cells with

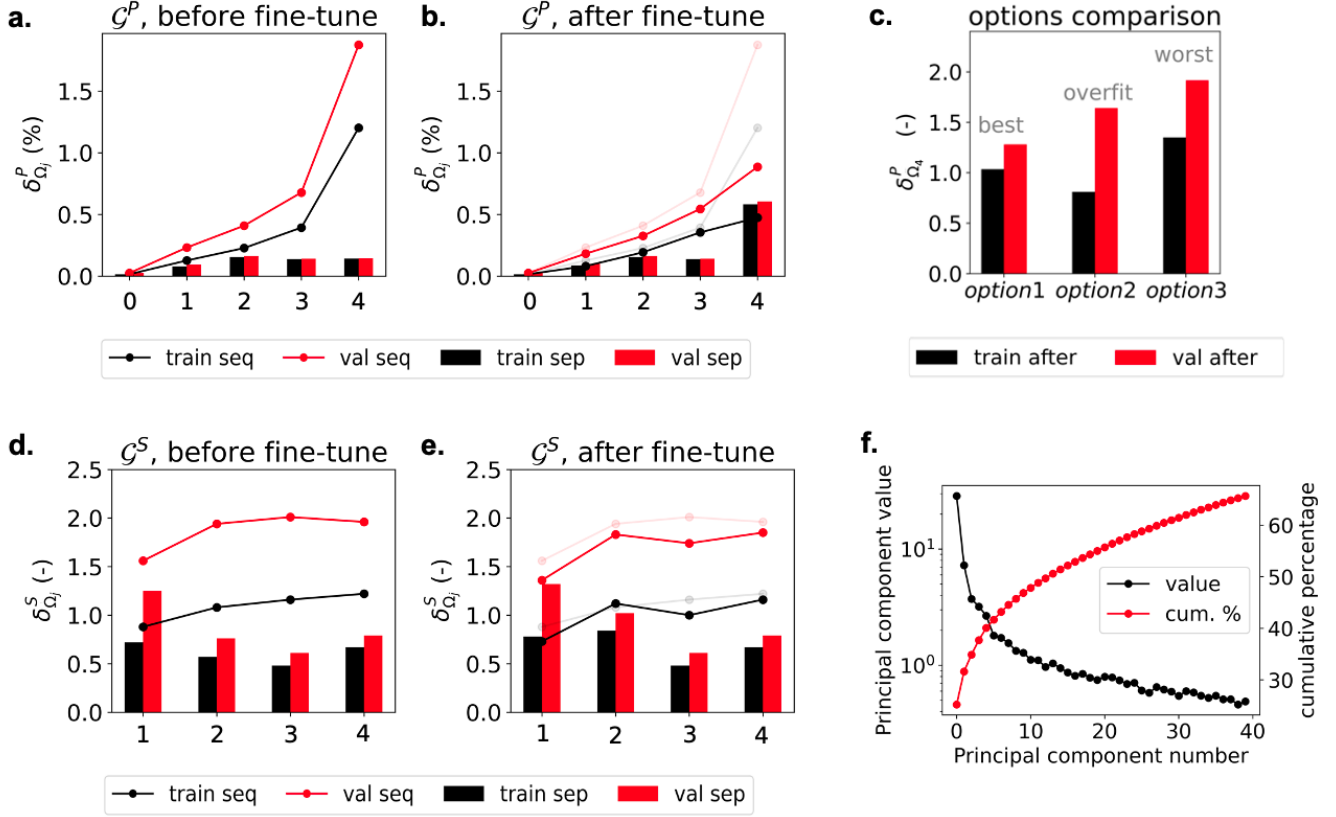


**Figure 5. Fine-tuning.** Each model’s separate and sequential error for **a.** pressure buildup before fine-tuning, **b.** pressure buildup after fine-tuning, **d.** gas saturation before fine-tuning, and **e.** gas saturation after fine-tuning. On the legend, ‘seq’ denotes sequential prediction, ‘sep’ denotes separate prediction. The transparent lines indicate the before fine-tune error. **e.** Training and validation set  $\delta_4^P$  of fine-tuning using Option 1 to 3. **f.** Principle component number and cumulative percentage of the 40 strongest rank for  $\mathcal{G}_3^P$ ’s error.

zero gas saturation; taking an average with these zero predictions leads to an overestimation of the gas saturation accuracy.  $\delta_S$  is a more strict metric focusing on the error within the plume.

For pressure buildup, we introduce relative error  $\delta^P$ :

$$\delta^P = \frac{1}{n_{\Omega}n_T} \sum_{t \in T} \sum_{i \in \Omega} \frac{|P_{t,i} - \hat{P}_{t,i}|}{P_{t,max}} \quad (2)$$

Here  $P$  is the ground truth pressure buildup given by numerical simulation,  $\hat{P}$  is the predicted pressure buildup,  $P_{t,max}$  is the maximum reservoir pressure buildup at time  $t$ ,  $n_{\Omega}$  is the number of cells in  $\Omega$ , and  $n_T$  is the number time steps. This metric is commonly used for evaluating reservoir pressure buildup<sup>30,42</sup>.

### Fine-tuning procedure

**Separate vs. sequential prediction.** As described in Algorithm 1, during inference, the input for each model

in levels 1 to 4 includes the  $\hat{S}$  or  $\hat{P}$  predicted by their corresponding coarser-level model. However, during training, the inputs are constructed by ground truth numerical simulation data. The discrepancy in training and inference leads to error accumulation, especially for the models that appear later in the prediction sequence.

To investigate this effect, we introduce two ways to evaluate each model: (1) separate prediction using the ground truth input taken from the numerical simulation (as in training), and (2) sequential prediction using predicted values from the coarser level as input (as in inference). Figure 5 a compares the average relative pressure buildup  $\delta_{\Omega_j}^P$  for each model using both separate and sequential prediction methods. Unlike  $\delta^P$ ,  $\delta_{\Omega_j}^P$  focuses on the ability of each model to produce outputs similar to the training data, defined as:



$$\delta_{\Omega_j}^P = \frac{1}{n_T n_{\Omega_j}} \sum_{t \in T} \sum_{i \in \Omega_j} \frac{|P_{t,i} - \hat{P}_{t,i}|}{P_{t,max}}. \quad (3)$$

Figure 5 a shows that all models have low errors and negligible overfitting when using separate predictions. However, with sequential prediction,  $\delta_{\Omega_j}^P$  quickly accumulates, going from coarser to finer-level models. The validation error of level 4 using sequential prediction increased by 13 times compared to separate predictions.

Similarly, for the gas saturation, the plume gas saturation error  $\delta_{\Omega_j}^S$  for each model is defined as:

$$\delta_{\Omega_j}^S = \frac{1}{\sum I_{t,i}} \sum_{t \in T} \sum_{i \in \Omega_j} |S_{t,i} - \hat{S}_{t,i}|$$

$$I_{t,i} = 1 \quad \text{if} \quad (S_{t,i} > 0.01) \cup (|\hat{S}_{t,i}| > 0.01) \quad (4)$$

Figure 5 d compares  $\delta_{\Omega_j}^S$  using separate versus sequential prediction. We observed less error accumulation for gas saturation than pressure buildup, which indicates that the prediction of gas saturation does not rely as heavily on coarser-level models.

**Random perturbation.** To reduce the error accumulation, we explored several fine-tuning techniques to improve generalizability using the level 4 pressure prediction as an example. To fine-tune  $\mathcal{G}_4^P$ , we add a perturbation to the ground truth input,  $P'_{3,i} = P_{3,i} + \zeta_i$  where  $i$  represents a sample taken from the training set. We defined the coarser-level model's error in the training set as  $\epsilon_3 = \hat{P}_3 - P_3$ , and explore three configurations of perturbation  $\zeta_i$ .

- Option 1:  $\zeta_i = \epsilon_{3,j}$  - randomly sample an instance from  $\epsilon_3$ .
- Option 2:  $\zeta_i = \epsilon_{3,i}$  - choose the error corresponding to the specific training sample (i.e., fine-tune with the predicted label  $\hat{P}_{3,i}$ ).
- Option 3:  $\zeta_i \sim \mathcal{N}(\mu_{\epsilon_3}, \sigma_{\epsilon_3})$  - generate a random Gaussian error using the mean and standard deviation of  $\epsilon_3$ .

As shown in Figure 5 c, Option 1 provides the best validation set performance with the smallest overfitting. By providing a randomly sampled noise instance from  $\epsilon_3$  with each training data, we let the finer-level models become aware of the presence of a structured error and learn to filter it out. Option 2 gives the best training set error but is significantly overfitted. Interestingly, Option

3 leads to the largest errors in both the training and validation set despite being a commonly used machine learning technique for introducing randomness.

We applied Option 1 to  $\mathcal{G}_1^P$ ,  $\mathcal{G}_4^P$ ,  $\mathcal{G}_1^S$ , and  $\mathcal{G}_2^S$ . After fine-tuning, sequential prediction errors are reduced for both pressure buildup and gas saturation (Figure 5 b and e). For pressure buildup, we observe a dramatic improvement on level 4, where the validation error decreased by more than 50%.

**Structure of prediction error.** We hypothesize that the FNO model's predictions and errors lie in a perturbed low-dimensional manifold in the output function spaces due to its structure. To verify our hypothesis, we analyzed the functional principle components on error  $\epsilon_3$ <sup>50</sup>. As shown in Figure 5 f, only a few principal components are needed to describe nearly a third of the error. Gaussian noised functions did not improve prediction because the Gaussian noise resides in an infinite-dimensional space, whereas the actual error only lives in a small linear sub-space.

## Web application

The trained Nested FNO model will be hosted at publicly accessible web application <https://ccsnet.ai> to provide real-time pressure buildup and gas saturation predictions upon the publication of this manuscript.

## Code and data availability

The python code for the Nested FNO model architecture and the data set used in training will be available at <https://github.com/gegewen/nestfno> upon the publication of this manuscript.

## References

1. NAS. *Negative Emissions Technologies and Reliable Sequestration* (National Academies Press, 2018).
2. Pruess, K., Oldenburg, C. M. & Moridis, G. Tough2 user's guide version 2. Tech. Rep., Lawrence Berkeley National Lab.(LBNL), Berkeley, CA (United States) (1999).
3. Blunt, M. J. *Multiphase flow in permeable media: A pore-scale perspective* (Cambridge university press, 2017).

4. Pruess, K. & Garcia, J. Multiphase flow dynamics during co<sub>2</sub> disposal into saline aquifers. *Environ. Geol.* **42**, 282–295 (2002).
5. Doughty, C. Investigation of CO<sub>2</sub> plume behavior for a large-scale pilot test of geologic carbon storage in a saline formation. *Transp. porous media* **82**, 49–76 (2010).
6. Wen, G. & Benson, S. M. CO<sub>2</sub> plume migration and dissolution in layered reservoirs. *Int. J. Greenh. Gas Control.* **87**, 66–79, DOI: [10.1016/j.ijggc.2019.05.012](https://doi.org/10.1016/j.ijggc.2019.05.012) (2019).
7. Pruess, K. & Müller, N. Formation dry-out from co<sub>2</sub> injection into saline aquifers: 1. effects of solids precipitation and their mitigation. *Water Resour. Res.* **45** (2009).
8. André, L., Peysson, Y. & Azaroual, M. Well injectivity during co<sub>2</sub> storage operations in deep saline aquifers—part 2: Numerical simulations of drying, salt deposit mechanisms and role of capillary forces. *Int. J. Greenh. Gas Control.* **22**, 301–312 (2014).
9. Chadwick, R. *et al.* Geological reservoir characterization of a co<sub>2</sub> storage site: The utsira sand, sleipner, northern north sea. *Energy* **29**, 1371–1381 (2004).
10. NETL. Best Practices: Risk Management and Simulation for Geologic Storage Projects (2017).
11. Bramble, J. H., Ewing, R. E., Pasciak, J. E. & Schatz, A. H. A preconditioning technique for the efficient solution of problems with local grid refinement. *Comput. Methods Appl. Mech. Eng.* **67**, 149–159 (1988).
12. Eigestad, G. T. *et al.* Geological modeling and simulation of co<sub>2</sub> injection in the johansen formation. *Comput. Geosci.* **13**, 435–450 (2009).
13. Faigle, B., Helmig, R., Aavatsmark, I. & Flemisch, B. Efficient multiphysics modelling with adaptive grid refinement using a mpfa method. *Comput. Geosci.* **18**, 625–636 (2014).
14. Kamashev, A. & Amanbek, Y. Reservoir simulation of co<sub>2</sub> storage using compositional flow model for geological formations in frio field and precaspian basin. *Energies* **14**, 8023 (2021).
15. Callas, C. *et al.* Criteria and workflow for selecting depleted hydrocarbon reservoirs for carbon storage. *Appl. Energy* **324**, 119668 (2022).
16. Strandli, C. W., Mehnert, E. & Benson, S. M. CO<sub>2</sub> plume tracking and history matching using multi-level pressure monitoring at the Illinois basin - Decatur project. *Energy Procedia* **63**, 4473–4484, DOI: [10.1016/j.egypro.2014.11.483](https://doi.org/10.1016/j.egypro.2014.11.483) (2014).
17. Nghiem, L., Shrivastava, V., Kohse, B., Hassam, M. & Yang, C. Simulation and optimization of trapping processes for co<sub>2</sub> storage in saline aquifers. *J. Can. Petroleum Technol.* **49**, 15–22 (2010).
18. Zhang, Z. & Agarwal, R. K. Numerical simulation and optimization of co<sub>2</sub> sequestration in saline aquifers for vertical and horizontal well injection. *Comput. Geosci.* **16**, 891–899 (2012).
19. Kou, Z., Wang, H., Alvarado, V., McLaughlin, J. F. & Quillinan, S. A. Method for upscaling of co<sub>2</sub> migration in 3d heterogeneous geological models. *J. Hydrol.* 128361 (2022).
20. Cavanagh, A. & Ringrose, P. Simulation of co<sub>2</sub> distribution at the in salah storage site using high-resolution field-scale models. *Energy Procedia* **4**, 3730–3737 (2011).
21. Zhu, Y. & Zabarar, N. Bayesian deep convolutional encoder–decoder networks for surrogate modeling and uncertainty quantification. *J. Comput. Phys.* **366**, 415–447 (2018).
22. Mo, S., Zhu, Y., Zabarar, N., Shi, X. & Wu, J. Deep convolutional encoder-decoder networks for uncertainty quantification of dynamic multiphase flow in heterogeneous media. *Water Resour. Res.* **55**, 703–728 (2019).
23. Tang, M., Liu, Y. & Durlofsky, L. J. A deep-learning-based surrogate model for data assimilation in dynamic subsurface flow problems. *J. Comput. Phys.* **413**, 109456 (2020).
24. Wen, G., Tang, M. & Benson, S. M. Towards a predictor for CO<sub>2</sub> plume migration using deep neural networks. *Int. J. Greenh. Gas Control.* **105**, 103223, DOI: [10.1016/j.ijggc.2020.103223](https://doi.org/10.1016/j.ijggc.2020.103223) (2021).
25. Wen, G., Hay, C. & Benson, S. M. CCSNet: a deep learning modeling suite for CO<sub>2</sub> storage. *Adv. Water Resour.* 104009, DOI: <https://doi.org/10.1016/j.advwatres.2021.104009> (2021).
26. Kovachki, N. *et al.* Neural operator: Learning maps between function spaces. *arXiv preprint arXiv:2108.08481* (2021).

27. Li, Z. *et al.* Multipole graph neural operator for parametric partial differential equations. *arXiv preprint arXiv:2006.09535* (2020).
28. Li, Z. *et al.* Neural operator: Graph kernel network for partial differential equations. *arXiv preprint arXiv:2003.03485* (2020).
29. Li, Z. *et al.* Fourier neural operator for parametric partial differential equations. *arXiv preprint arXiv:2010.08895* (2020).
30. Wen, G., Li, Z., Azizzadenesheli, K., Anandkumar, A. & Benson, S. M. U-fno—an enhanced fourier neural operator-based deep-learning model for multiphase flow. *Adv. Water Resour.* **163**, 104180 (2022).
31. Data: Sleipner co2 reference dataset, published via the co2 datashare online portal administrated by sintef as, DOI: [10.11582/2020.00004](https://doi.org/10.11582/2020.00004).
32. Data: Illinois state geological survey (isgs), illinois basin - decatur project (ibdp) co2 injection monitoring data, april 30, 2021. midwest geological sequestration consortium (mgsc) phase iii data sets. doe cooperative agreement no. de-fc26-05nt42588, DOI: [10.11582/2022.00017](https://doi.org/10.11582/2022.00017).
33. EPA. Geologic sequestration of carbon dioxide - underground injection control (uic) program class vi well area of review evaluation and corrective action guidance (2013). 816-R-13-005.
34. Schlumberger. Eclipse reservoir simulation software reference manual (2014).
35. Pawar, R. J. *et al.* The national risk assessment partnership’s integrated assessment model for carbon storage: A tool to support decision making amidst uncertainty. *Int. J. Greenh. Gas Control.* **52**, 175–189 (2016).
36. Kumar, N. & Bryant, S. Optimizing injection intervals in vertical and horizontal wells for co2 sequestration. In *SPE Annual Technical Conference and Exhibition* (OnePetro, 2008).
37. Yin, Z., Siahkoobi, A., Louboutin, M. & Herrmann, F. J. Learned coupled inversion for carbon sequestration monitoring and forecasting with fourier neural operators. *arXiv preprint arXiv:2203.14396* (2022).
38. Jiang, Z., Tahmasebi, P. & Mao, Z. Deep residual u-net convolution neural networks with autoregressive strategy for fluid flow predictions in large-scale geosystems. *Adv. Water Resour.* 103878 (2021).
39. Wu, H. & Qiao, R. Physics-constrained deep learning for data assimilation of subsurface transport. *Energy AI* **3**, 100044 (2020).
40. Kadeethum, T. *et al.* A framework for data-driven solution and parameter estimation of pdes using conditional generative adversarial networks. *Nat. Comput. Sci.* **1**, 819–829 (2021).
41. Tang, M., Liu, Y. & Durlofsky, L. J. Deep-learning-based surrogate flow modeling and geological parameterization for data assimilation in 3d subsurface flow. *Comput. Methods Appl. Mech. Eng.* **376**, 113636 (2021).
42. Tang, H. *et al.* A deep learning-accelerated data assimilation and forecasting workflow for commercial-scale geologic carbon storage. *Int. J. Greenh. Gas Control.* **112**, 103488 (2021).
43. Raissi, M., Perdikaris, P. & Karniadakis, G. E. Physics-informed neural networks: A deep learning framework for solving forward and inverse problems involving nonlinear partial differential equations. *J. Comput. Phys.* **378**, 686–707 (2019).
44. Fuks, O. & Tchelepi, H. Physics based deep learning for nonlinear two-phase flow in porous media. In *ECMOR XVII*, vol. 2020, 1–10 (European Association of Geoscientists & Engineers, 2020).
45. Almajid, M. M. & Abu-Elseid, M. O. Prediction of porous media fluid flow using physics informed neural networks. *J. Petroleum Sci. Eng.* 109205 (2021).
46. Fraces, C. G. & Tchelepi, H. Physics informed deep learning for flow and transport in porous media. In *SPE Reservoir Simulation Conference* (OnePetro, 2021).
47. Haghighat, E., Amini, D. & Juanes, R. Physics-informed neural network simulation of multiphase poroelasticity using stress-split sequential training. *Comput. Methods Appl. Mech. Eng.* **397**, 115141 (2022).
48. Dong, K. & Neumann, C. J. On the relative motion of binary tropical cyclones. *Mon. weather review* **111**, 945–953 (1983).
49. Jin, S., Roche, K. J., Stetcu, I., Abdurrahman, I. & Bulgac, A. The lise package: Solvers for static and time-dependent superfluid local density approximation equations in three dimensions. *Comput. Phys. Commun.* **269**, 108130 (2021).

50. Blanchard, G., Bousquet, O. & Zwald, L. Statistical properties of kernel principal component analysis. *Mach. Learn.* **66**, 259–294 (2007).
51. Pini, R., Krevor, S. C. & Benson, S. M. Capillary pressure and heterogeneity for the CO<sub>2</sub>/water system in sandstone rocks at reservoir conditions. *Adv. Water Resour.* **38**, 48–59 (2012).
52. Remy, N., Boucher, A. & Wu, J. *Applied Geostatistics with SGeMS: A User's Guide* (Cambridge University Press, 2009).

## Acknowledgements

The authors gratefully acknowledge Yanhua Yuan from ExxonMobil for many helpful conversations and suggestions. G.W. and S.B. gratefully acknowledge the support by ExxonMobil through the Strategic Energy Alliance at Stanford University and the Stanford Center for Carbon Storage. Z.L. gratefully acknowledges the financial support from the Kortschak Scholars, PIMCO Fellows, and Amazon AI4Science Fellows programs. A.A. is supported in part by Bren endowed chair.

## Author contributions statement

G.W. Conceptualization, Methodology, Software, Data acquisition, Data curation, Formal analysis, Investigation, Validation, Visualization, Writing – original draft, Writing – review & editing. Z.L. Methodology, Investigation, Validation, Writing – original draft, Writing – review & editing. Q.L. Data acquisition. K.A. Methodology, Software, Investigation, Validation, Writing – review & editing. A.A. Funding acquisition, Supervision, Writing – review & editing. S.B. Conceptualization, Formal analysis, Funding acquisition, Methodology, Resources, Supervision, Writing – review & editing.

## Additional information

**Competing interests** The authors declare no competing interests.



# Supplementary Material to "Accelerating Carbon Capture and Storage Modeling using Fourier Neural Operators"

## 1 Governing equation

We consider the immiscible multiphase flow problem with  $\text{CO}_2$  and water in the context of  $\text{CO}_2$  geological storage. The multiphase flow is governed by the basic mass balance equations, and the general forms of mass accumulations are written as<sup>2</sup>:

$$\frac{\partial M^\eta}{\partial t} = -\nabla \cdot \mathbf{F}^\eta + q^\eta, \quad (5)$$

where  $\eta$  denotes component of  $\text{CO}_2$  or *water*,  $\mathbf{F}$  denotes the flux, and  $q$  denotes the source term. For each component, the mass accumulation term is summed over phase  $p = w$  (wetting) or  $n$  (non-wetting)

$$M^\eta = \phi \sum_p S_p \rho_p X_p^\eta. \quad (6)$$

Here  $\phi$  is the porosity,  $S_p$  is the saturation of phase  $p$ , and  $X_p^\eta$  is the mass fraction of component  $\eta$  in phase  $p$ . Component *water* is the wetting phase in most storage formations with siliciclastic rocks<sup>51</sup>. Meanwhile,  $\text{CO}_2$  and *water* have mutual solubility; therefore, a small amount of  $\text{CO}_2$  dissolves into the wetting phase, and a small amount of *water* vaporizes into the non-wetting phase.

For both components, the advective mass flux  $\mathbf{F}^\eta|_{adv}$  is obtained by summing over phases  $p$ ,

$$\mathbf{F}^\eta|_{adv} = \sum_p X^\eta \mathbf{F}_p = \sum_p X^\eta \left( -k \frac{k_{r,p} \rho_p}{\mu_p} (\nabla P_p - \rho_p \mathbf{g}) \right) \quad (7)$$

where each individual phase flux  $\mathbf{F}_p$  is governed by the multiphase flow extension of Darcy's law derived from the Navier-Stokes equation<sup>3</sup>.  $k$  denotes the absolute permeability,  $k_{r,p}$  is the relative permeability of phase  $p$  that non-linearly depends on  $S_p$ ,  $\mu_p$  is the viscosity of phase  $p$  that depends on  $P_p$ , and  $\mathbf{g}$  is the gravitational acceleration.

Due to the effect of capillarity, the fluid pressure  $P_p$  of each phase is

$$P_n = P_w + P_c \quad (8)$$

$$P_w = P_w \quad (9)$$

where the capillary pressure  $P_c$  is a non-linear function of  $S_p$ . Additionally, porosity  $\phi$ , density  $\rho_p$ , and the flow composition in Equation 6 and Equation 7 are also non-linear functions that depend on  $P_p$ .

## 2 Local Grid Refinement

We inject  $\text{CO}_2$  into a 3D saline formation with multiple vertical injection wells. The reservoir is  $160,000 \text{ m} \times 160,000 \text{ m} \times 100 \text{ m}$  with a dip angle along the  $x$ -axis. The large spatial domain is chosen to mimic saline formations with infinite-acting boundaries; no flow boundary conditions are used for the top and bottom of the formation. On the global level (level 0), we used a grid resolution of  $1,600 \text{ m} \times 1,600 \text{ m} \times 20 \text{ m}$  to simulate the entire reservoir domain.

Each reservoir has 1 to 4 injection wells. Around each injection well, we apply high-resolution local refinements to capture the multi-phase flow processes. Specifically, since  $\text{CO}_2$  is lighter than the formation fluid, the  $\text{CO}_2$  plume will migrate upward due to gravity forces. Large grid thicknesses, such as the 20 m at level 0, will suppress gravity override and leads to underestimation of the plume footprint<sup>6</sup>. In addition, the injection of  $\text{CO}_2$  leads to rapid near-well pressure buildup. Using large lateral grids will greatly underestimate the maximum pressure buildup. Large lateral grids will also ignore the dry-out zone near the injection wells<sup>8</sup>. Therefore, we gradually refine the grid cell size from  $1,600 \text{ m} \times 1,600 \text{ m} \times 20 \text{ m}$  to  $20 \text{ m} \times 20 \text{ m} \times 2 \text{ m}$ , and named each refinement from level 1 being the coarsest to level 4 being the finest. The injection wells are placed in the middle of level 4. The level 1

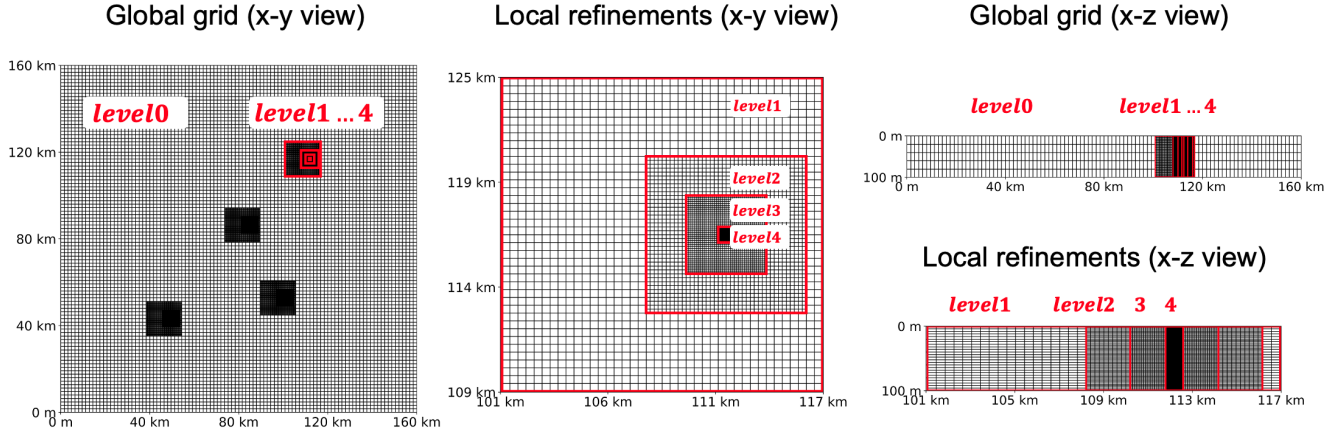


**Figure 6.** Grid visualizations for the entire reservoir (x-y view), local refinements around the injection well (x-y view), entire reservoir (x-z view) and local refinements around the injection well (x-z view).

**Table 1.** Spatial dimension, cell size, matrix dimension, and the number of cells for level 0-4 grids.

	Spatial dimension (m)	Cell size (m)	Matrix dim	# of cells
level 0	160,000×160,000×100	1,600×1,600×20	100×100×5	50,000
level 1	16,000×16,000×100	400×400×4	40×40×25	40,000
level 2	8,000×8,000×100	200×200×2	40×40×50	80,000
level 3	4,000×4,000×100	100×100×2	40×40×50	80,000
level 4	800×800×100	20×20×2	40×40×50	80,000

refinements never overlap with each other. Table 1 summarizes detailed information for each level, and Figure 6 provides visualizations for levels 0 to 4 grid in a 4-well reservoir.

We designed the LGRs so that the CO<sub>2</sub> plume always stays within levels 1 to 4. Specifically, levels 2 to 4 are placed on the right-hand side of level 1 (Figure 6) because the simulated reservoir dips downwards along the  $x$ -axis. CO<sub>2</sub> is more likely to migrate up-dip, especially for high permeable reservoirs. This design ensures the CO<sub>2</sub> gas saturation plume never enters the level 0 grids.

### 3 Data set generation

To demonstrate the potential to make the Nested FNO a general-purpose numerical simulator alternative, we sampled a wide range of inputs to cover most realistic scenarios for CO<sub>2</sub> injection into saline formations. This differs from most ‘surrogate’ modeling approaches with fixed reservoir conditions and permeability maps constrained by a prior. The following sections introduce the sampling ranges for reservoir conditions, injection schemes, and permeability fields. Sampling ranges are summarized in Table 2.

#### 3.1 Reservoir conditions

We sample the reservoir depth from 800 m to 4,500 m. For the upper bound, injecting deeper than 800 m ensures that the CO<sub>2</sub> plume stays in the supercritical state. For the lower bound, our sampling range is deeper than commonly used ranges for CCS ( $\sim 3,000$  m) to include deep offshore formations such as in the Gulf of Mexico. Reservoir temperatures are calculated according to the reservoir depth and a geothermal gradient variable, which we sampled from 15 to 35 C° per km. Within each formation, we assume isothermal conditions. Deeper reservoirs lead to higher initial pressures and temperatures, which in turn introduce a more diverse range of CO<sub>2</sub> properties (e.g., density, solubility, and viscosity).

Our data set also considers a range of reservoir dip angles. Since CO<sub>2</sub> is lighter than formation fluid, it would naturally migrate up-dip. The influence on plume migration is particularly significant for large dip angles and

**Table 2.** Variables parameters and sample ranges used for generating the input data set.

Variable type	Sampling parameter	Distribution	Unit
Permeability map	$x$ -axis correlation	$X \sim \mathcal{U}[800, 4000]$	m
	$y$ -axis correlation	$X \sim \mathcal{U}[800, 4000]$	m
	$z$ -axis correlation	$X \sim \mathcal{U}[4, 20]$	m
	reservoir permeability mean	$X \sim \mathcal{U}[4.09, 5.01]$	ln mD
	reservoir permeability std	$X \sim \mathcal{U}[0.25, 1]$	ln mD
Reservoir cond.	Reservoir center depth	$X \sim \mathcal{U}[800, 4500]$	m
	Geothermal gradient	$X \sim \mathcal{U}[15, 35]$	°C/km
	Dip angle	$X \sim \mathcal{U}[0, 2]$	°C/km
Injection design	# of wells	$n \in \{1, 2, 3, 4\}$	-
	Injection rate	$X \sim \mathcal{U}[0.5, 2]$	MT/y
	Perforation thickness	$X \sim \mathcal{U}[20, 100]$	m
	Perforation location	Randomly placed	-

high permeability formations. We sampled dip angles from 0 to 2° to consider this effect and then discarded the reservoirs that are shallower than 800m or deeper than 4,500 m. The dip angle is applied to the  $x$ -axis, and the initial hydrostatic pressure in each cell is assigned according to the cell depth. Figure 1 in the main manuscript document demonstrates a reservoir with four injection wells, where the deepest and shallowest injection depths are more than 1,000 meters apart vertically due to the dip angle. As a result, the plume migration and pressure buildup around these two wells are influenced by significantly different reservoir conditions.

### 3.2 Injection scenarios

We randomly place one to four wells in each reservoir. Each well is at least 5,000 m away from the reservoir boundaries to avoid pressure influence. Each well has a constant injection rate sampled from 0.5 to 2 MT/year over 30 years. We also sampled perforation lengths from 20 m to 100 m for each injection well and randomly placed the perforation interval along the well.

### 3.3 Permeability fields

To generate the 3D heterogeneous permeability fields, we used a modified version of Stanford Geostatistical Modeling Software (SGeMS)<sup>52</sup> to create random media according to 3D spatial correlations. For each permeability field, we sampled random correlation lengths on the  $x$ -axis from 800 m to 4,000 m,  $y$ -axis from 800 m to 4,000 m, and  $z$ -axis from 4 m to 20 m. The random field is generated at the resolution of level 2 and subsequently up-sampled for levels 0-1 level and down-sampled for levels 3-4 using tri-linear interpolation. Note that the up-sampling and down-sampling of the permeability map is *not* performed to capture the flow characteristics. Instead, it simply re-grids the random field to another resolution while maintaining the spatial correlations for training. This is different from an ‘up-scaling’ context, where the coarser permeability field is expected to capture the flow of the finer permeability field.

Then, we scaled the distribution of each permeability field according to a pair of the randomly sampled  $\ln$  permeability mean and  $\ln$  permeability standard deviation (Table 2). The maximum cell permeability in the data set is 14 Darcy, and the minimum is kept at 0.1 mD. Figure 1 (main text) shows an example of the permeability field.

## 4 Numerical simulation setting

We use a full physics numerical simulator, ECLIPSE (e300), to solve the governing PDEs. ECLIPSE uses the finite difference method with upstream weighting for spatial discretization and the fully implicit method for temporal discretization<sup>34</sup>. ECLIPSE uses the non-conforming grid technique to simulate the domain with local grid refinement. We do not explicitly simulate molecular diffusion and hydrodynamic dispersion. However, numerical simulation results include some unavoidable numerical diffusion and dispersion resulting from finite difference gradient approximation. Since we applied LGRs around each injection well, the number of cells in each reservoir ranges

from  $\sim 0.3$  million to  $\sim 1$  million, depending on the number of injection wells. We run each ECLIPSE numerical simulation on 20 parallel Intel® Xeon® E5-2640 CPU using Stanford University's HPC cluster. The average ECLIPSE run times are summarized in Table 6 (b).

Corey's curve and Leverette-J function scaling is used for relative permeability and capillary pressure. In our previous work, we demonstrated that these curves could also be variables in deep learning models by sampling the irreducible water saturation and the scaling factor for capillary pressure curves<sup>25,30</sup>. We did not vary rock properties in this study; however, they can be incorporated using the same approach.

After running the numerical simulation, we extract 24-time snapshots for gas saturation and pressure buildup during 30 years of injection. We sampled the time snapshots with higher frequencies at the beginning of the injection and lower frequencies near the end of the injection. This technique is commonly used in numerical simulations to guide engineering decisions.

The data set includes 3011 cases for level 0 and 7374 for levels 1-4 because each reservoir can have one to four injection wells. We then split the data into training/validation/testing sets at an 8/1/1 ratio, which gives us 2408/301/302 for level 0 and 5916/731/727 for LGR models.

## 5 Fourier Neural Operator

The computational domain of the Nested Fourier Neural Operator (FNO) is a 3D space with time,  $D = \Omega \times T$ , where  $T$  is the time interval of 30 years and  $\Omega$  is the 3D spatial domain. The Nested FNO consists of nine FNOs for five levels of sub-domains  $\Omega = \{\Omega_0, \Omega_1, \dots, \Omega_4\}$ , where each subdomain corresponds to a level of grid refinement. The inputs and outputs are functions defined on the 4D domain from the corresponding function spaces  $\mathcal{A} = \mathcal{U} = L^\infty(D)$ .

Each FNO model learns an infinite-dimensional-space mapping from a finite collection of input-output observations (i.e. data set  $\{a_j, u_j\}_{j=1}^N$ ). We use  $n$ -point space-time discretization  $D_j = \{\xi_1, \dots, \xi_n\} \subset D$ , where  $\xi = (\omega, t)$ , to numerically represent  $a_j|_{D_j} \in \mathbb{R}^{n \times d_a}$  and  $u_j|_{D_j} \in \mathbb{R}^{n \times d_u}$  so that  $a_j$  consists of the input coefficient functions and  $u_j$  consists of output functions of gas saturation  $S$  and pressure buildup  $P$ . FNO is a type of neural operator (Definition 1) where we use the Fourier integral kernel operator (Definition 2) as the linear integral operator to achieve efficient and accurate training.

**Definition 1** (Neural operator). A  $L$ -layered neural operator  $\mathcal{G}_\theta$  is defined as:

$$\mathcal{G}_\theta := \mathcal{Q} \circ (W_L + \mathcal{K}_L) \circ \dots \circ \sigma(W_1 + \mathcal{K}_1) \circ \mathcal{P}, \quad (10)$$

where  $\mathcal{P}$  is a pointwise operator that expands the input function to a higher co-dimension space, parameterized with  $\mathcal{P} : \mathbb{R}^{d_a} \rightarrow \mathbb{R}^{d_{l=1}}$ . In each layer for  $l \in 1 \dots L$ ,  $\mathcal{K}$  is a linear integral operator,  $W$  is a linear matrix operator, and  $\sigma$  is a non-linear activation. Lastly,  $\mathcal{Q}$  is a pointwise operator that projects the function to the output space, parameterized with  $\mathcal{Q} : \mathbb{R}^{d_{l=L}} \rightarrow \mathbb{R}^{d_u}$ .

All parameters in  $\mathcal{P}$ ,  $\mathcal{K}_l$ ,  $W_l$ , and  $\mathcal{Q}$  are learned through training. By stacking multiple neural operator layers,  $\mathcal{G}_\theta$  can approximate the mapping of high dimensional functions with strong non-linearity.

**Definition 2** (Fourier integral kernel operator). An integral kernel operator  $\mathcal{K}$  is defined by

$$(\mathcal{K}(v_l))(\xi) = \int_D \kappa(\xi, \xi') v_l(\xi') d\xi', \quad \forall \xi' \in D. \quad (11)$$

To efficiently parameterize kernel  $\mathcal{K}$ , the FNO method<sup>29</sup> represents  $v_l$  in the Fourier space to directly parameterize  $\kappa$  by its Fourier coefficients:

$$(\mathcal{K}(v_l))(\xi) = \mathcal{F}^{-1}(R \cdot \mathcal{F}(v_l))(\xi), \quad \forall \xi \in D. \quad (12)$$

where  $R$  is the Fourier transform of a periodic function  $\kappa$ ,  $\mathcal{F}$  denotes a Fourier transform of a function  $f : D \rightarrow \mathbb{R}^c$  and  $\mathcal{F}^{-1}$  is its inverse. To further improve computational efficiency and reduce memory consumption, we truncate



the Fourier series at a maximum number of modes ( $k_{max}$ ), and then parameterize  $R$  with the truncated Fourier coefficients. Therefore, we can implement  $R$  using a linear parameterization as

$$(R \cdot \mathcal{F}(v_l))_{k,i} = \sum_{j=1}^c R_{k,i,j}(\mathcal{F}(v_l))_{k,j}, \quad \forall k = 1, \dots, k_{max}, i = 1, \dots, c. \quad (13)$$

Using the Fourier integral kernel operator as  $\mathcal{K}_{1...L}$  gives us the FNO architecture. Since the data is provided on uniform grids, we utilize the Fast Fourier Transform (FFT) to implement and approximate the Fourier transform. The speed and low memory requirement of FFT make our proposed method computationally fast with a significantly low memory footprint. We denote FNO with  $\mathcal{G}$  (in short of  $\mathcal{G}_\theta$ ) throughout this paper.

We summarized the parameters in the following tables: level 0 (Table 3), level 1 (Table 4), and levels 2 to 4 (Table 5). We used 4 Fourier layers for each sub-model with a width of 28. The modes ( $t, x, y, z$ ) are (4, 20, 20, 2) for the level 0 and (6, 10, 10, 10) for levels 1 to 4.

**Table 3.** FNO model parameters for the level 0 level. The `Padding` denotes a padding operator that accommodates the non-periodic boundaries; `Linear` denotes the linear transformation to lift the input to the high dimensional space, and the projection back to original space; `Fourier4d` denotes the 4D Fourier operator; `Conv1d` denotes the bias term; `Add` operation adds the outputs together; `GELU` denotes a Gaussian Error Linear Units layer.

Layer	Operation	Output Shape
Input	-	(24, 100, 100, 5, 8)
Padding	Padding (8)	(40, 116, 116, 21, 8)
Lifting	Linear	(40, 116, 116, 21, 28)
Fourier 1	Fourier4d/Conv1d/Add/GELU	(40, 116, 116, 21, 28)
Fourier 2	Fourier4d/Conv1d/Add/GELU	(40, 116, 116, 21, 28)
Fourier 3	Fourier4d/Conv1d/Add/GELU	(40, 116, 116, 21, 28)
Fourier 4	Fourier4d/Conv1d/Add	(40, 116, 116, 21, 28)
De-padding	Depadding (8)	(24, 100, 100, 5, 28)
Projection 1	Linear	(24, 100, 100, 5, 112)
Projection 2	Linear	(24, 100, 100, 5, 1)

**Table 4.** FNO model parameters for the level 1 level. The `Padding` denotes a padding operator that accommodates the non-periodic boundaries; `Linear` denotes the linear transformation to lift the input to the high dimensional space, and the projection back to original space; `Fourier4d` denotes the 4D Fourier operator; `Conv1d` denotes the bias term; `Add` operation adds the outputs together; `GELU` denotes a Gaussian Error Linear Units layer.

Layer	Operation	Output Shape
Input	-	(24, 40, 40, 25, 9)
Padding	Padding (8)	(40, 56, 56, 41, 9)
Lifting	Linear	(40, 56, 56, 41, 28)
Fourier 1	Fourier4d/Conv1d/Add/GELU	(40, 56, 56, 41, 28)
Fourier 2	Fourier4d/Conv1d/Add/GELU	(40, 56, 56, 41, 28)
Fourier 3	Fourier4d/Conv1d/Add/GELU	(40, 56, 56, 41, 28)
Fourier 4	Fourier4d/Conv1d/Add	(40, 56, 56, 41, 28)
De-padding	Depadding (8)	(24, 40, 40, 25, 28)
Projection 1	Linear	(24, 40, 40, 25, 112)
Projection 2	Linear	(24, 40, 40, 25, 1)

## 6 Training procedure

We use Nvidia A100-SXM GPUs for the training. Each model fits into the GPU with a batch size of one. We use the relative  $l_2$ -loss function for the training because it provides normalized loss across cases, leading to excellent

**Table 5.** FNO model parameters for levels 2-4. The Padding denotes a padding operator that accommodates the non-periodic boundaries; Linear denotes the linear transformation to lift the input to the high dimensional space, and the projection back to original space; Fourier4d denotes the 4D Fourier operator; Conv1d denotes the bias term; Add operation adds the outputs together; GELU denotes a Gaussian Error Linear Units layer.

Layer	Operation	Output Shape
Input	-	(24, 40, 40, 50, 9)
Padding	Padding (8)	(40, 56, 56, 66, 9)
Lifting	Linear	(40, 56, 56, 66, 28)
Fourier 1	Fourier4d/Conv1d/Add/GELU	(40, 56, 56, 66, 28)
Fourier 2	Fourier4d/Conv1d/Add/GELU	(40, 56, 56, 66, 28)
Fourier 3	Fourier4d/Conv1d/Add/GELU	(40, 56, 56, 66, 28)
Fourier 4	Fourier4d/Conv1d/Add	(40, 56, 56, 66, 28)
De-padding	Depadding (8)	(24, 40, 40, 50, 28)
Projection 1	Linear	(24, 40, 40, 50, 112)
Projection 2	Linear	(24, 40, 40, 50, 1)

gradient propagation compared to a vanilla  $l_2$ -loss or RMSE error. Each model was trained for 30 and 40 epochs and fine-tuned for around 10 epochs until the validation set error plateaus. Instead of relative  $l_2$ -loss, we monitored the plume gas saturation error (main text, Equation 3) and relative pressure buildup error (main text, Equation 4) on the validation set as an indicator of when to stop training. We do not monitor the relative  $l_2$ -loss because it is normalized over the sample's norm, making the magnitudes carry different meanings among different refinement levels.

Note that the numerical simulator domains at levels 0 to 3 are annular because they do not include information at the finer refinement levels. To help with the FNO learning (which prefers continuous functions), we construct the continuous training domains by down-sampling the information from the finer LGRs to populate the annular domains. Our experiments show that the continuous training domains provide more efficient learning than the annular simulator domains. The down-sampled information is only used during the training and is not reported in the final prediction. Figure 7 shows the simulator domain and training domain at each level.

## 7 Speedup analysis

Once the Nested FNO model is trained, we can directly use it as a numerical simulator alternative for CO<sub>2</sub> gas saturation and pressure buildup prediction in 3D saline formations. Therefore, we compared the ML model prediction time with the numerical simulation time to compute the computational efficiency speed-up. We summarized each model's training and prediction times in the Nested FNO in Table 6 (a). The machine learning models are evaluated on Nvidia A100-SXM GPUs. All models take  $\sim 0.005$  s to evaluate. The prediction time depends on the number of injection wells:  $t_{total} = t_{global} + n_{well} \times \sum_{i=1}^4 t_i$ . We run each ECLIPSE numerical simulation on 20 parallel Intel® Xeon® E5-2640 CPU using Stanford HPC cluster. The run time also depends on the number of injection wells since more wells lead to more cells. Table 6 (b) shows that the Nested FNO provides  $4 \times 10^5$  to  $7 \times 10^5$  times speed-up compared to traditional numerical simulation. Interestingly, four-well cases with larger cell counts have the most significant speed-up. The advantage of using Nested FNO is more prominent with higher dimensional cases. The advantage of using Nested FNO is more prominent with higher dimensional cases. In addition, Nested FNO can predict pressure buildup or gas saturation separately, whereas numerical simulation always calculates all variables regardless of whether they are needed. The speed-up is calculated considering separate predictions for gas saturation and pressure buildup.

## 8 Accuracy summary

Table 7 shows an accuracy summary for train, validation, and test sets in the simulator domain, the training domain with separate prediction, and the training domain with sequential prediction.

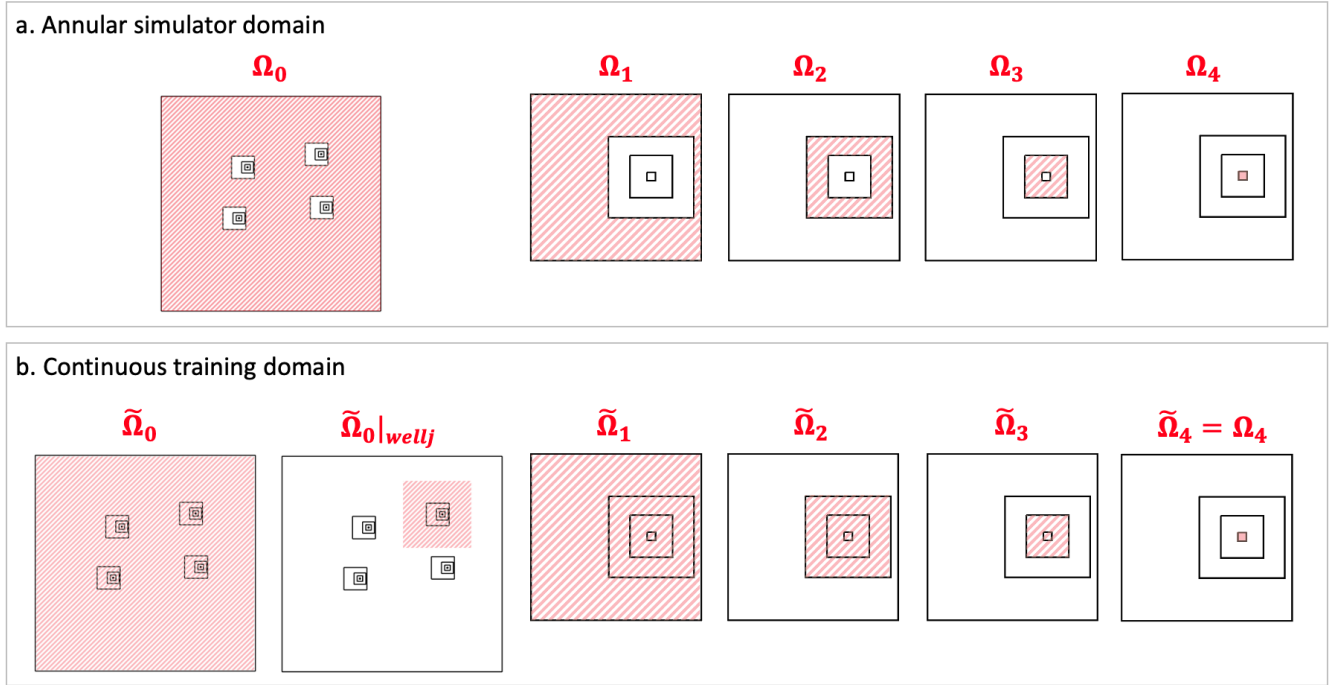


**Figure 7.** Simulator domain and training domain for each level

## 9 Probabilistic assessment

We use Nested FNO to conduct probabilistic assessments on CO<sub>2</sub> plume footprint and maximum pressure buildup. We consider CO<sub>2</sub> injection through 4 injection wells where each well injects at a 1MT/year rate. All wells inject through a perforation located at the bottom 20 meters of the reservoir. We generated 1,000 permeability realizations where the permeability average and standard deviation for each map are 85mD and 100mD, respectively. The correlation lengths on  $x$ ,  $y$ , and  $z$  directions are 2000, 4000, and 20 meters, respectively. The 10 realizations shown in Figure 4 (main text) were taken from the same injection well.

CO<sub>2</sub> plume footprint is defined as the area of land under the separate phase CO<sub>2</sub> plume, which has a gas saturation larger than 0.01. We calculate the plume footprint using the Nested FNO's gas saturation prediction and the  $xy$ -cross section area of each grid cell. The plume footprint reported in Figure 4 (main text) is the reservoir's total plume footprint; the maximum pressure buildup reported in Figure 4 (main text) is the reservoir's maximum.

**Table 6.** (a). Prediction time, training time, and the number of parameters for levels 0-4 models. The prediction time is calculated based on an average of 250 runs. (b) Speed up calculation for ECLIPSE vs. Nested FNO. We show the number of cells and average run time of the ECLIPSE simulation and the Nested FNO prediction time, both averaging over 250 cases. The speed-up is calculated for predicting gas saturation and pressure buildup separately.

**(a)**

Model	Prediction (s)	Training (hr/epoch)	# of parameter
level 0	0.005	0.96	80,288,461
level 1	0.005	1.43	150,534,889
level 2	0.005	2.20	150,534,889
level 3	0.005	2.20	150,534,889
level 4	0.005	2.20	150,534,889

**(b)**

# of Wells	# of Cells	ECLIPSE (hr)	Nested FNO (s)	Speed-up
1	296,300	2.75	0.025	$3.96 \times 10^5$
2	542,600	6.43	0.045	$5.14 \times 10^5$
3	788,900	11.00	0.065	$6.09 \times 10^5$
4	1,035,200	15.93	0.085	$6.75 \times 10^5$

**Table 7.** Accuracy summary for train, validation, and test sets in the simulator domain, the training domain with separate prediction, and the training domain with sequential prediction.

**(a) Pressure buildup**

Simulator domain	Train (%)	Validation (%)	Test (%)
$\delta^P$	0.34	0.48	0.47
Training domain, separate	Train (%)	Validation (%)	Test (%)
$\delta_0^P$	0.02	0.02	0.02
$\delta_1^P$	0.09	0.11	0.10
$\delta_2^P$	0.15	0.16	0.16
$\delta_3^P$	0.14	0.14	0.14
$\delta_4^P$	0.42	0.47	0.45
Training domain, sequential	Train (%)	Validation (%)	Test (%)
$\delta_0^P$	0.02	0.02	0.02
$\delta_1^P$	0.08	0.15	0.16
$\delta_2^P$	0.19	0.31	0.30
$\delta_3^P$	0.38	0.50	0.51
$\delta_4^P$	0.59	0.81	0.82

**(b) Gas saturation**

Simulator domain	Train (%)	Validation (%)	Test (%)
$\delta^S$	1.16	1.81	1.79
Training domain, separate	Train (%)	Validation (%)	Test (%)
$\delta_1^S$	0.78	1.32	1.27
$\delta_2^S$	0.84	1.02	1.00
$\delta_3^S$	0.48	0.61	0.61
$\delta_4^S$	0.67	0.79	0.74
Training domain, sequential	Train (%)	Validation (%)	Test (%)
$\delta_1^S$	0.73	1.36	1.39
$\delta_2^S$	1.17	1.88	1.91
$\delta_3^S$	1.00	1.74	1.77
$\delta_4^S$	1.16	1.85	1.82